

Air Force Institute of Technology

AFIT Scholar

Student Publications

4-2024

Nowcasting Solar EUV Irradiance With Photospheric Magnetic Fields and the Mg II Index

Kara L. Kniezewski

Samuel J. Schonfeld

Carl J. Henney

Follow this and additional works at: <https://scholar.afit.edu/studentpub>



Part of the [Atomic, Molecular and Optical Physics Commons](#), and the [Electromagnetics and Photonics Commons](#)



RESEARCH ARTICLE

10.1029/2023SW003772

Key Points:

- Improved nowcast models for commonly used extreme ultraviolet (EUV) and far ultraviolet (FUV) solar irradiance bands
- Utilization of well-calibrated MgII observations decreases the error between the modeled and observed EUV values
- Real-time EUV observations are not required to correct and improve the EUV irradiance models

Correspondence to:

K. L. Kniezewski,
karakniezewski@gmail.com

Citation:

Kniezewski, K. L., Schonfeld, S. J., & Henney, C. J. (2024). Nowcasting solar EUV irradiance with photospheric magnetic fields and the Mg II index. *Space Weather*, 22, e2023SW003772. <https://doi.org/10.1029/2023SW003772>

Received 25 OCT 2023

Accepted 28 MAR 2024

Nowcasting Solar EUV Irradiance With Photospheric Magnetic Fields and the Mg II Index

Kara L. Kniezewski¹ , Samuel J. Schonfeld² , and Carl J. Henney²
¹Air Force Institute of Technology, Wright-Patterson Air Force Base, OH, USA, ²Air Force Research Lab/Space Vehicles Directorate, Kirtland AFB, NM, USA

Abstract A new method to nowcast spectral irradiance in extreme ultraviolet (EUV) and far ultraviolet (FUV) bands is presented here, utilizing only solar photospheric magnetograms and the Mg II index (i.e., the core-to-wing ratio). The EUV and FUV modeling outlined here is a direct extension of the SIFT (Solar Indices Forecasting Tool) model, based on Henney et al. (2015, <https://doi.org/10.1002/2014sw001118>). SIFT estimates solar activity indices using the earth-side solar photospheric magnetic field sums from global magnetic maps generated by the ADAPT (Air Force Data Assimilative Photospheric Flux Transport) model. Utilizing strong and weak magnetic field sums from ADAPT maps, Henney et al. (2015, <https://doi.org/10.1002/2014sw001118>) showed that EUV & FUV observations can also be well modeled using this technique. However, the original forecasting method required a recent observation of each SIFT model output to determine and apply a 0-day offset. The new method described here expands the SIFT and ADAPT modeling to nowcast the observed Mg II index with a Pearson correlation coefficient of 0.982. By correlating the Mg II model-observation difference with the model-observation difference in the EUV & FUV channels, Mg II can be used to apply the 0-day offset correction yielding improvements in modeling each of the 37 studied EUV & FUV bands. With daily global photospheric magnetic maps and Mg II index observations, this study provides an improved method of nowcasting EUV & FUV bands used to drive thermospheric and ionospheric modeling.

Plain Language Summary Ultraviolet irradiance from the Sun can create variability in Earth's atmosphere and cause problems, for example, with satellite communication and their orbital paths. However, we are limited in measuring solar ultraviolet irradiance since it must be observed from space and therefore models of the irradiance are important. In this paper, we present an improved way to model ultraviolet irradiance using solar magnetic fields and a well-calibrated solar activity proxy. We find that models of the irradiance improve when the proxy is used to correct daily variations compared to models driven using just the magnetic fields.

1. Introduction

Solar irradiance, specifically the ultraviolet (UV) band vacuum UV (VUV; 0.1–200 nm) which includes X-ray UV (XUV; 0.1–10 nm), extreme UV (EUV; 10–120 nm) and far UV (FUV; 120–200 nm), is an important driver for modeling variability in the Earth's upper atmosphere. For example, the solar EUV flux causes ionization, dissociation, and excitation of the atoms and molecules in the terrestrial upper atmosphere (Lilensten et al., 2008). All of these interactions lead to heating, and this solar irradiance both creates the ionosphere and is the main source of energy in the thermosphere (Fuller-Rowell et al., 2004). The atmospheric variability induced by changes in the solar EUV irradiance can impact radio communications (due to an enhanced ionosphere e.g., Klobuchar, 1985; McNamara, 1985) and atmospheric drag on satellites (due to increased density at high altitudes e.g., De LaFontaine & Garg, 1982). Because of these impacts, real-time knowledge of solar irradiance is necessary to drive nowcast models of the terrestrial upper atmosphere (e.g., Goncharenko et al., 2021).

However, measurements of the solar EUV irradiance have serious limitations because these wavelengths are absorbed in the Earth's upper atmosphere, so they must be observed from space. While such measurements began in the 1960s, this spectral range has been inconsistently observed and there are large gaps in both time and spectral coverage when no observatories were taking measurements (Pesnelli, 2016). Furthermore, even when measurements exist, they are notoriously difficult to calibrate due to instrumental degradation (e.g., R. A. Hock et al., 2012). Because of these observational difficulties, there is significant benefit to modeling rather than observing the solar EUV irradiance spectrum.

Solar EUV originates in the solar atmosphere from plasma at a wide variety of temperatures, from 50 kK in the upper chromosphere to 10 MK in the corona, and typically increases with solar activity. Many solar irradiance models use one (e.g., Richards et al., 1994) or more (e.g., P. C. Chamberlin et al., 2020) activity proxies and correlate them with individual channels of EUV irradiance spectra. Then, simply by measuring the proxy, select EUV and FUV spectral bands can be estimated. Two commonly used proxies are the solar 10.7 cm (2.8 GHz) radio flux (Covington, 1947; Tapping, 2013), abbreviated as $F_{10.7}$ and the Mg II core-to-wing ratio (often referred to as the Mg II Index, and hereinafter referred to as Mg II; Heath & Schlesinger, 1986).

Besides using proxies similar to $F_{10.7}$, it is also possible to drive an EUV model using solar magnetic field measurements (e.g., full-disk magnetograms and global magnetic maps) since the magnetic fields provide the energy to heat the solar atmosphere that produces the EUV irradiance. Henney et al. (2012); Henney et al. (2015, hereafter Henney2012 and Henney2015, respectively) used earth-side weak and strong solar photospheric magnetic field sums from global magnetic maps to estimate irradiance in EUV bands, along with $F_{10.7}$. Similar work by Warren et al. (2021) utilized more bins in the magnetic field strength combined with principle component analysis and demonstrated similar success modeling $F_{10.7}$, Mg II, and selected EUV emission lines.

This paper expands on the nowcasting components of Henney2012 and Henney2015 by focusing on Mg II rather than $F_{10.7}$ and using it to correct EUV nowcasts. The Henney2015 EUV forecast method required a recent EUV observation to determine and apply a 0-day (nowcast) correction. The method described here instead uses the Mg II model to estimate corrections to EUV nowcast models. The data used in this study are described in Section 2. The addition of the Mg II modeling, its use as a corrective factor to the Solar Indices Forecasting Tool (SIFT), and the results of this study are described in Section 3. We provide a summary of the results in Section 4.

2. Solar Data Sources

Beginning on 22 January 2002, the Thermosphere Ionosphere Mesosphere Energetic and Dynamics (TIMED) Solar EUV Experiment (SEE) observations define the start of our investigation period. Figure 1 shows the daily trend of solar activity during our period of investigation, from the maximum of Solar Cycle 23 through 2010 and the Cycle 23/24 minimum. This date range matches Henney2012 and Henney2015.

2.1. Mg II Index

For this study we use the Mg II daily composite index from the University of Bremen (Snow et al., 2014), available online at http://www.iup.uni-bremen.de/gome/solar/MgII_composite.dat. The Bremen composite data set (Skupin et al., 2005) includes daily indices back to 1978. The solar Mg II Index is derived by taking the ratio between the spectral irradiance of the Mg II h and k absorption lines near 280 nm and the nearby background solar continuum (Heath & Schlesinger, 1986). Mg II varies with solar activity on many timescales (Dudok de Wit et al., 2008, 2009) and performs well as a proxy for solar activity and for some EUV emission (i.e., 25.0–35.0 nm Viereck et al., 2001). Since Mg II is generated from a ratio of measurements taken with the same instrument, despite requiring a spacecraft UV observation, the Mg II index is robust against instrument degradation and aging. The Mg II data is recorded in a single 50 s observation window daily at 1200 UT. No effort is made to remove the effects of solar flares in these data.

2.2. EUV and FUV Irradiance

The irradiance data used in this study are from the TIMED/SEE observations from the EUV Grating Spectrograph (EGS) and XUV Photometer System (XPS) (Woods et al., 1998). These data include low-resolution (~5 nm) diode measurements below 25 nm (XPS) and 0.4 nm resolution spectra between 25 and 195 nm (EGS) collected over ~3-min observation windows once per ~90-min orbit. We use the calibration version 11 EGS level 3 and XPS level 4 data products for this study. These data are averaged over a day to create this daily cadence data and flares have been removed. Additionally, we de-spike EUV Band 1 (i.e., range 0.05–0.4 nm) values above 0.7 $\mu\text{W}/\text{m}^2$, replacing them with the average of the previous and following days' data points. Four data points (i.e., large "spikes") are removed from Band 1 across the entire 9-year period.

For this study, we re-bin these data into 37 bands between 0.05 and 175 nm shown in Table 1. These include the 22 bands defined in Solomon and Qian (2005) for input in general thermosphere and ionosphere models, plus 14 additional bands which cover the Shumann-Runge range (Torr et al., 1979), and the Lyman α line. While these 37

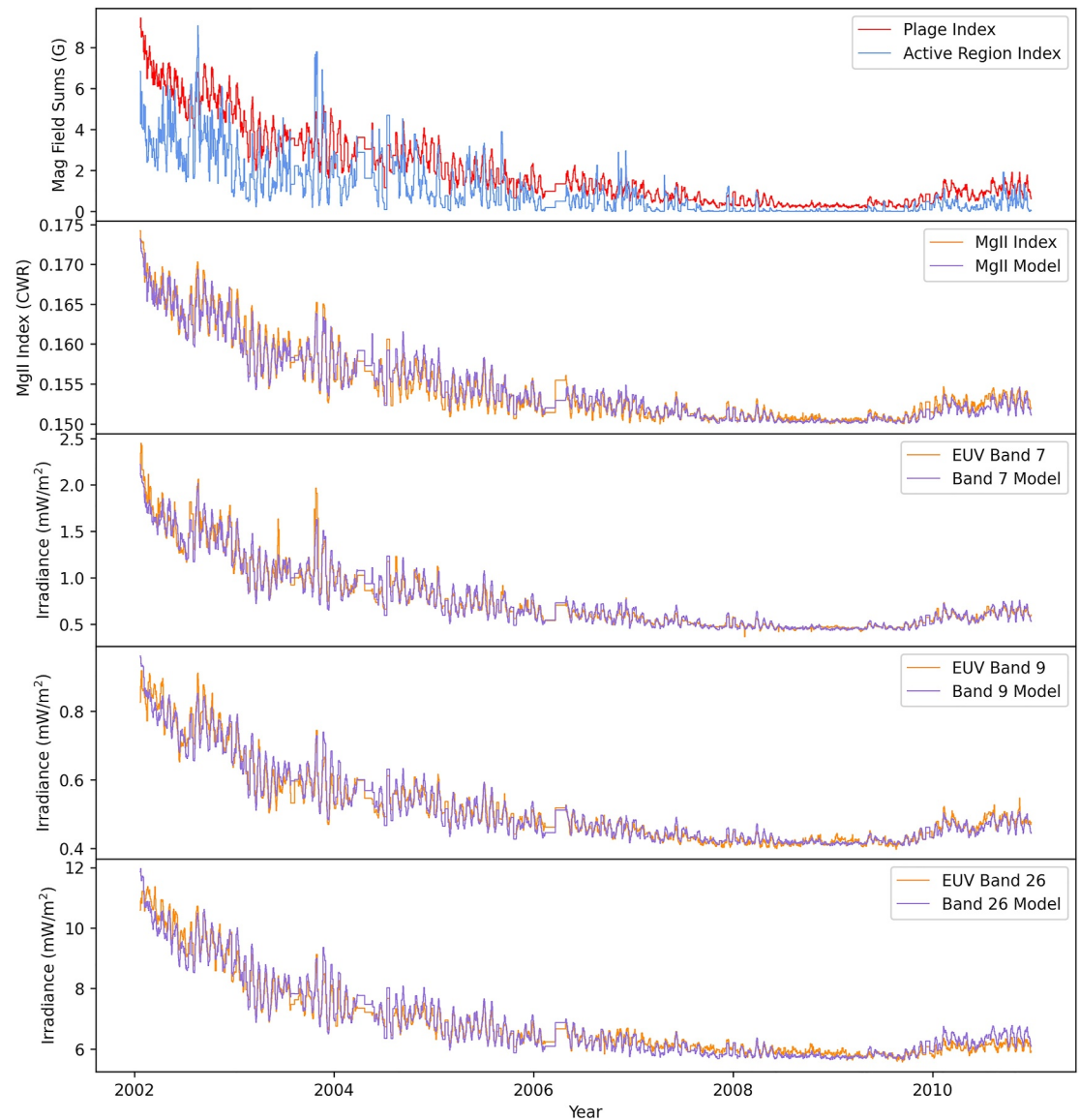


Figure 1. From top to bottom: the active and plage weighted magnetic sums, the Mg II nowcast model and observed values, and the Band 7 (15.5–22.4 nm), Band 9 (29.0–32.0 nm), and Band 26 (121.6 nm) EUV nowcast models and observed values. Note that the magnetic Plage Index variability, both long and short term, agrees with Mg II and the EUV Band 7, 9, and 26 time series over the full period. Similar figures for all 37 bands are available at Kniezewski et al. (2023).

bands include XUV, EUV, and FUV irradiance, we will refer to them all as EUV bands and the spectrum they cover as the EUV for simplicity. The emission sources for each band include atomic transitions from the chromosphere through the corona. Shorter wavelengths (i.e., <20 nm) are generally from coronal emission, and longer wavelengths (i.e., >50 nm) generally come from the chromosphere and upper transition region (Doschek & Feldman, 2010), although this is not a sharp distinction.

2.3. Photospheric Magnetic Field

Following Henney2012 and Henney2015, the magnetic field data used for this study are from global photospheric magnetic maps created by the ADAPT model (Arge et al., 2010, 2013; Hickmann et al., 2015). The ADAPT maps are generated by assimilating observations when available and applying surface flux transport based on Worden and Harvey (2000) to account for differential rotation, meridional circulation, and supergranulation flows

Table 1
EUV Irradiance Bands and Associated Correlation Coefficients

Band (n)	Range (nm)	r(Mg II)	$r(I_{model}^n)$	$r(I_{model}^n$ with offset)
1	0.05–0.4	0.845	0.865	0.866
2	0.4–0.8	0.920	0.927	0.931
3	0.8–1.8	0.965	0.969	0.973
4	1.8–3.2	0.975	0.976	0.981
5	3.2–7.0	0.976	0.977	0.982
6	7.0–15.5	0.976	0.977	0.982
7	15.5–22.4	0.977	0.978	0.983
8	22.4–29.0	0.980	0.979	0.985
9	29.0–32.0	0.982	0.978	0.985
10	32.0–54.0	0.975	0.974	0.980
11	54.0–65.0	0.948	0.942	0.951
12	65.0–79.8 (low)	0.937	0.933	0.942
13	65.0–79.8 (high)	0.945	0.937	0.948
14	79.8–91.3 (low)	0.978	0.974	0.981
15	79.8–91.3 (middle)	0.978	0.974	0.982
16	79.8–91.3 (high)	0.978	0.974	0.981
17	91.3–97.5 (low)	0.980	0.974	0.982
18	91.3–97.5 (middle)	0.981	0.975	0.983
19	91.3–97.5 (high)	0.979	0.971	0.981
20	97.5–98.7	0.955	0.957	0.961
21	98.7–102.7	0.978	0.975	0.981
22	102.7–105.0	0.977	0.972	0.979
23	105.0–110.0	0.982	0.982	0.987
24	110.0–115.0	0.982	0.981	0.986
25	115.0–120.0	0.714	0.671	0.736
26	121.6 (Lyman α)	0.981	0.977	0.985
27	120.0–125.0	0.975	0.956	0.976
28	125.0–130.0	0.985	0.976	0.987
29	130.0–135.0	0.985	0.979	0.987
30	135.0–140.0	0.983	0.981	0.987
31	140.0–145.0	0.974	0.973	0.978
32	145.0–150.0	0.963	0.955	0.965
33	150.0–155.0	0.961	0.962	0.966
34	155.0–160.0	0.962	0.962	0.966
35	160.0–165.0	0.962	0.951	0.963
36	165.0–170.0	0.941	0.930	0.942
37	170.0–175.0	0.918	0.902	0.918

Note. r(Mg II) is the correlation between the modeled band irradiance and the observed Mg II. $r(I_{model}^n)$ is the correlation between the modeled band irradiance and the observed band irradiance, and $r(I_{model}^n$ with offset) includes the Mg II correction term (i.e., Equation 5).

between observations. The ADAPT model generates 12 realizations of the photospheric magnetic field to represent the variable state of the Sun outside of the observed field of view. However, since the model nearside data is strongly dependent on the observations directly assimilated into the models, the difference in the magnetic field on the Earth-facing hemisphere in the 12 realizations is quite small. Therefore for simplicity, SIFT currently uses only the first realization of ADAPT to generate the magnetic sums.

The ADAPT sequence used in this study assimilates line-of-sight magnetograms from the Kitt Peak Vacuum Telescope (KPVT; Jones et al., 1992) and Vector Spectromagnetograph (VSM; Henney et al., 2009). For this paper, the VSM magnetograms used as input to ADAPT were reprocessed with improved calibration and new bias and scaling updates, as compared to the original VSM data used in Henney2012 and Henney2015. The recalibration resulted in changes depending on center-to-limb variation and field strength. These ground-based observations were obtained at irregular times, sometimes with many days between observations. For the model and observation comparison in this study, we applied a cubic spline interpolation to the TIMED/SEE EUV and Mg II daily indices to sample these series only when new data was assimilated into ADAPT.

3. EUV Nowcasts

3.1. SIFT: Solar Indices Forecasting Tool

The SIFT model uses empirical linear relationships to nowcast and forecast solar activity proxies and irradiance from photospheric magnetic fields. The fundamental assumption is that the magnetic field on the Earth-facing hemisphere of the Sun determines the observed solar irradiance. Following Henney2012 and Henney2015, the Earth-facing magnetic field in the ADAPT maps is summed into two bins corresponding to plage ($20 \text{ G} < B_r < 150 \text{ G}$), S_p , and active regions ($150 \text{ G} \leq B_r$), S_A . Although Henney2012 and Henney2015 started the plage bin at 25 G, we chose 20 G to remain consistent with the current SIFT implementation. The difference is also negligible to model performance. As outlined in Henney2012, the two sums are calculated as

$$S_p = \frac{1}{\sum \omega_\theta} \sum_{20\text{G} < |B_r| < 150\text{G}} |B_r| \omega_\theta \quad (1)$$

and

$$S_A = \frac{1}{\sum \omega_\theta} \sum_{|B_r| \geq 150\text{G}} |B_r| \omega_\theta, \quad (2)$$

where B_r is the radial magnetic field and ω_θ is an area weighting to account for the unequal pixel areas in the plate carée ADAPT map (180 latitude pixels by 360 longitude pixels). All of the sums are over only the Earth-facing pixels. An example ADAPT global magnetic map, generated with VSM magnetograms, is illustrated in Figure 2, where the Earth-facing side of the Sun is delineated by the white box and the regions with plage and active region fields

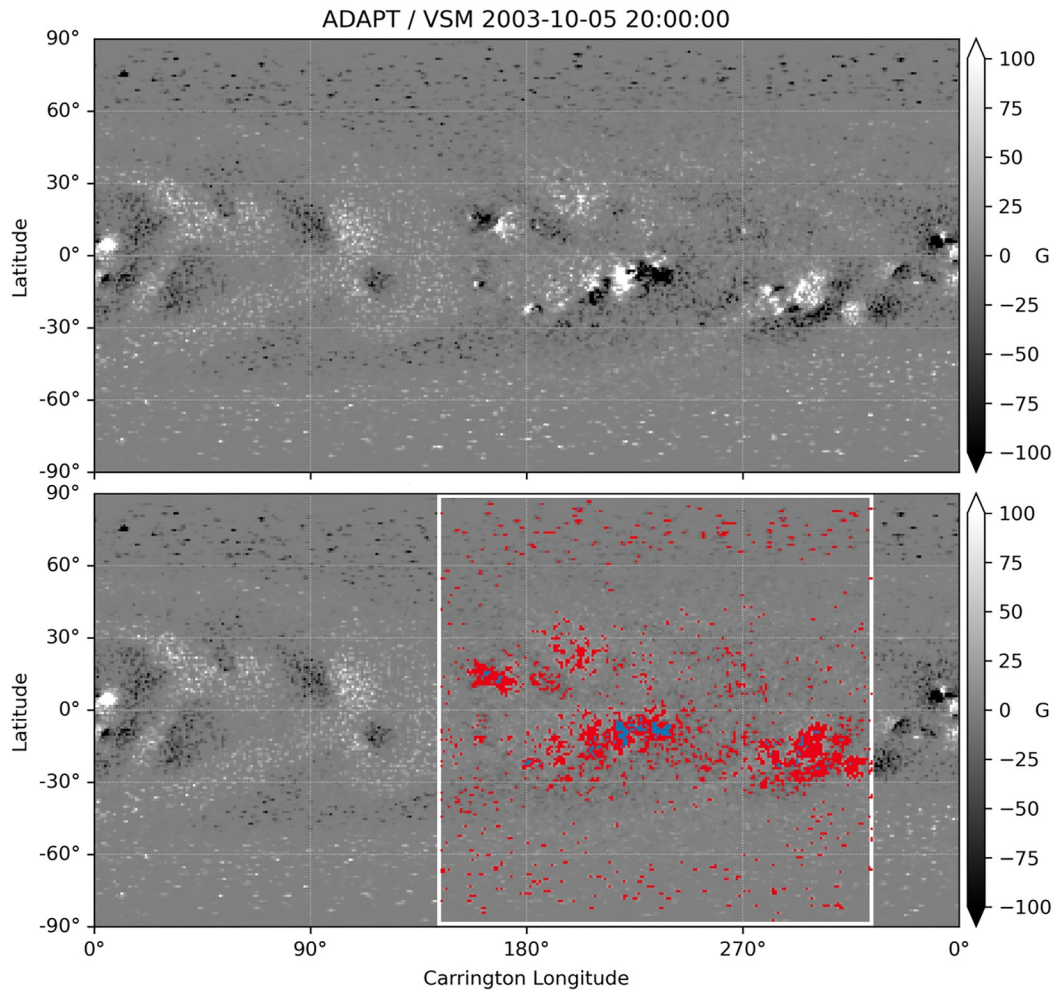


Figure 2. *Top:* An example ADAPT global photospheric magnetic map on 5 October 2003 at 20:00 UT, generated by data assimilating NSO SOLIS/VSM magnetograms. *Bottom:* The same ADAPT map with the Earth pointing side of the Sun delineated by the white box and the SIFT active region and plage fields highlighted in blue and red, respectively.

are highlighted in red and blue, respectively. We then use linear regression to determine the coefficients for a model of the following form:

$$I_{model}^n = m_0^n + m_1^n S_P + m_2^n S_A \quad (3)$$

where n is the solar index or irradiance band number modeled and m_0 , m_1 , and m_2 are best fit coefficients. In Henney2012 and Henney2015 these models were trained independently for nowcasts and forecasts out to seven days. In this work, we create only nowcast models, although the procedures described below should work equally well for forecasts.

3.2. Nowcasting the Mg II Index and EUV Irradiance

Using Equation 3, independent models are generated for Mg II and each of the 37 EUV bands using the entire 9-year data set. Timeseries of the magnetic sums, Mg II observations and model, and three EUV bands of interest observations and model are shown in Figure 1. Since it is impractical to display all 37 EUV bands, we chose to display Band 7 (15.5–22.4 nm) for its strong coronal lines, Band 9 (29.0–32.0 nm) which contains the strong He II 304 Å emission line, and Band 26 (121.6 nm) which is the Lyman-α line. Consistent with the findings in Henney2012 and Henney2015, both the Mg II and EUV time series have similar variability to the magnetic sums over

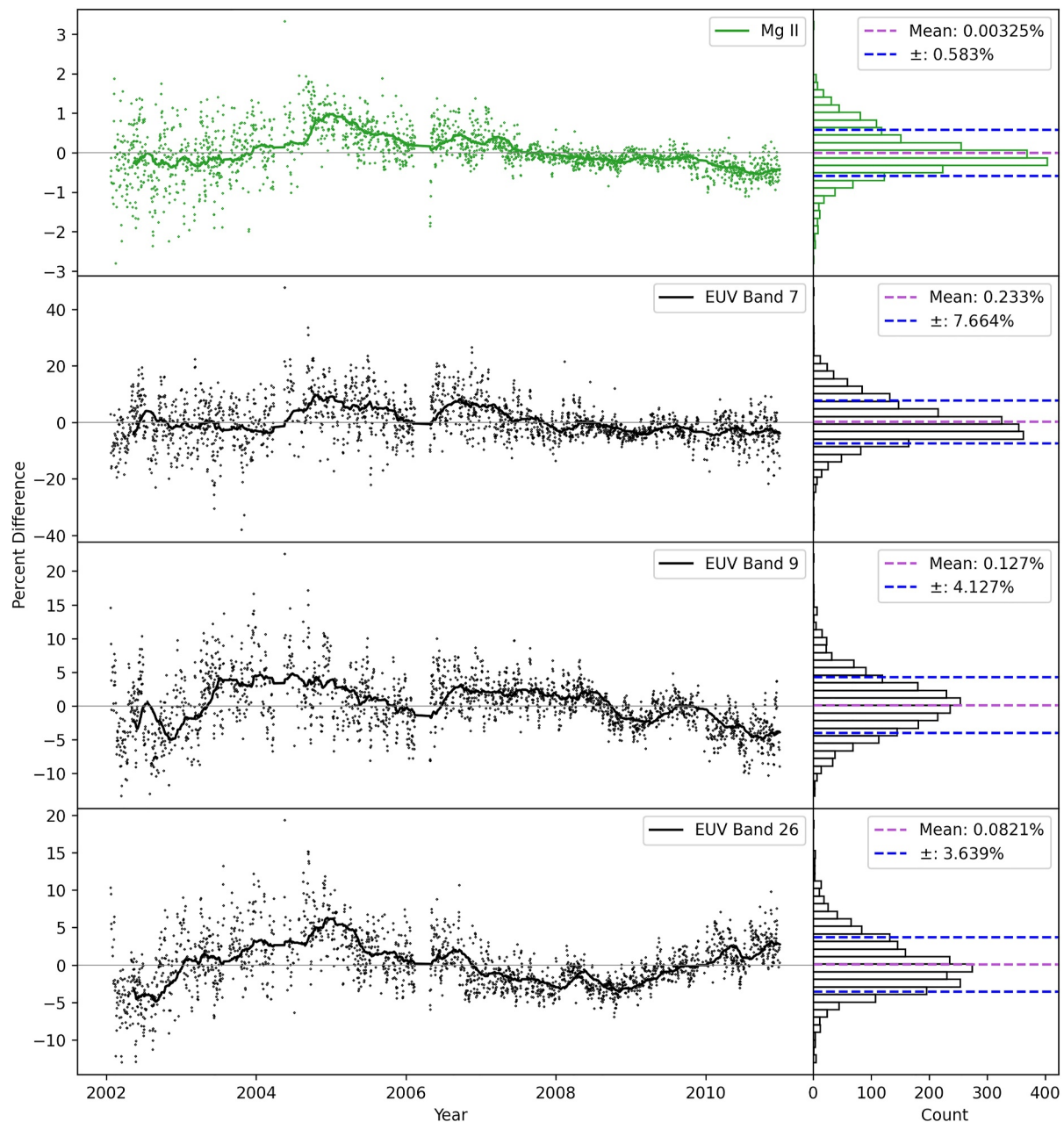


Figure 3. The daily (points) and 81-day running average difference between the modeled and observed Mg II (top) and EUV Bands 7, 9, and 26 plotted as a percent difference from the observed value. To the right of each time series is a histogram indicating the distribution of daily offsets over the entire data set. The mean (purple) and standard deviation (blue) for each band's offsets are included with each histogram. Notice that the Mg II and EUV offsets track each other well throughout the solar cycle.

all observed levels of solar activity. The simple multiple linear regression Mg II model reproduces the observed Mg II well with a Pearson correlation coefficient of 0.982. The correlation of the observed and modeled EUV Band 7 is 0.978, Band 9 is 0.978, and Band 26 is 0.977. The correlations of all the EUV bands is given in Table 1. Note that the $r(I_{model}^n)$ values in Table 1 slightly differ from Henney2012 and Henney2015. Since we chose to interpolate the Mg II and EUV timeseries to when new data was assimilated into ADAPT maps and the VSM magnetograms were recalibrated by NSO since Henney2012 and Henney2015, some variation in our model correlation values are expected. In general, the EUV bands perform similarly well, although there are some with

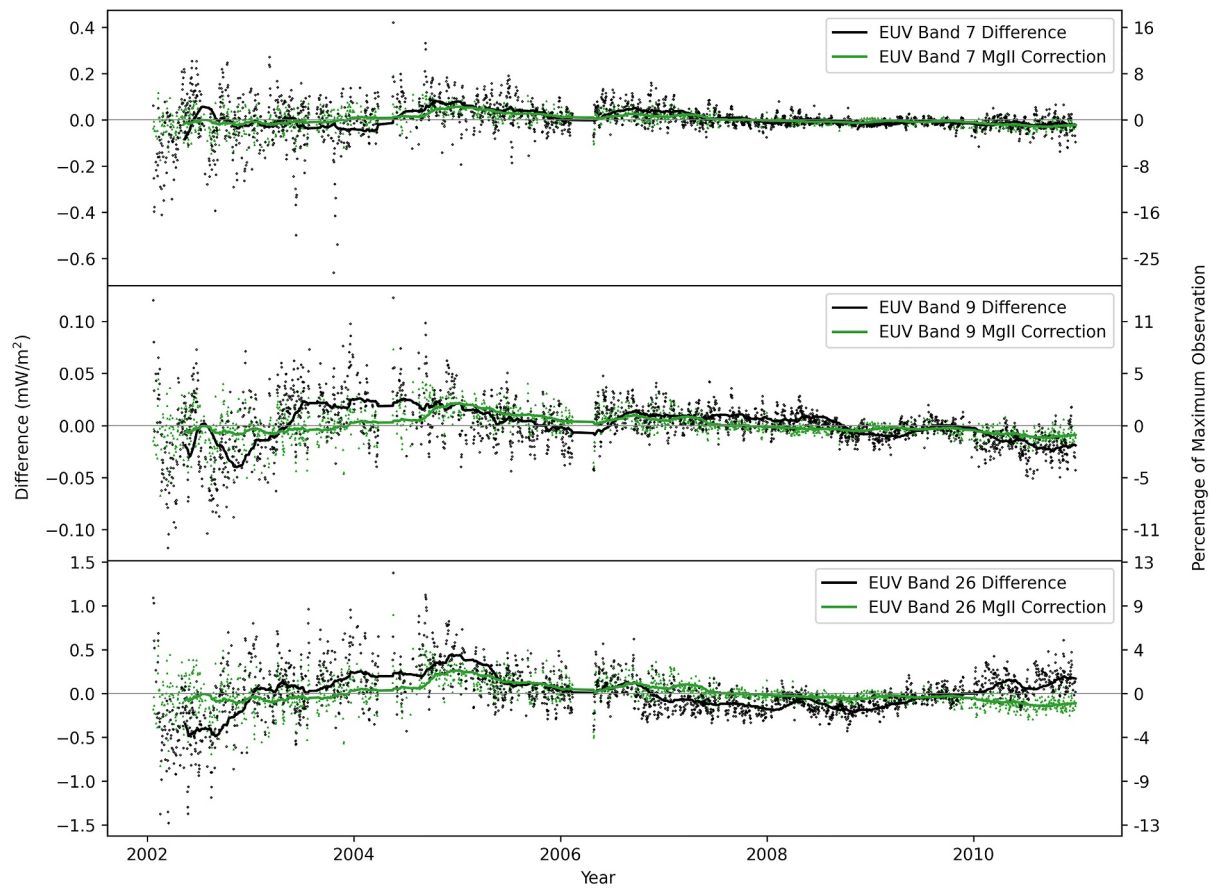


Figure 4. Plots of the difference between observed and modeled Bands 7, 9, and 26 EUV values, and the EUV difference models. The difference models were developed by comparing EUV to Mg II offset values.

notably lower correlation coefficients. Band 25, which has the lowest correlation of the 37 bands, is just blue-ward of Lyman α and the filter to ensure EGS does not saturate makes measuring this spectral range difficult (Woods et al., 2005). Meanwhile, Band 1 with the second worst correlation contains the highly variable soft X-ray (SXR) that is particularly sensitive to solar flares. All the other EUV bands have a Pearson correlation better than 0.9.

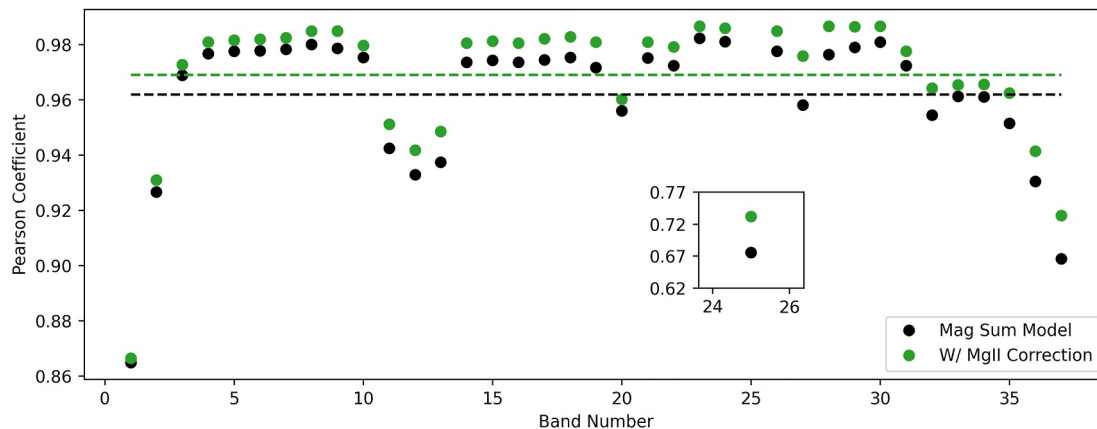


Figure 5. Pearson correlation coefficients which compare the relationship between each observed EUV spectral band and the nowcast models with (green) and without (black) a Mg II correction. Since Band 25 did not perform as well compared to the other bands, its Pearson coefficients are included on a separate, sub-graph to enhance the results of the other bands. The horizontal dashed lines indicate the average Pearson correlation coefficient across all bands (except band 25).

The difference between the models and observed values in the various bands are not random in time. Figure 3 shows both the daily (points) and long-term, 81-day trailing running average, trend (line) of the difference between the observed and modeled Mg II (top) and EUV Bands 7, 9, and 26. These time series demonstrate the long-term deviation of the models from observations (which are small) and are temporally correlated over the 9-year period displayed in Figure 3. The daily differences are typically largest during maximum solar magnetic activity when the irradiance is most variable. This is expected because both the magnetic sums and Mg II vary more during solar maximum than solar minimum, so the same relative difference results in larger absolute differences. Interestingly, the time-dependent long-term bias in all four of these models is largest at the intermediate activity levels during the decline of Solar Cycle 23.

3.3. EUV Nowcast Correction

The simple linear regression models applied in SIFT have a number of known limitations. Most fundamentally, while the magnetic field is responsible for solar activity (Petrie et al., 2021), the solar atmospheric response to photospheric magnetic fields is dynamic and non-linear (e.g., Tiwari et al., 2017), and may not always be well represented by a static model. Furthermore, solar EUV irradiance is often concentrated in active regions (depending on wavelength, see e.g., Kazachenko & Hudson, 2020), and the spatial information in the magnetic field is not included in the current SIFT modeling. Finally, the ADAPT maps that drive SIFT do not assimilate data near the limb (see Barnes et al., 2023; Hickmann et al., 2015) to reduce the introduction of artifacts from the line-of-sight magnetic field measurements that would otherwise be assumed to be radial (see, e.g., Harvey et al., 2007). This leads to a ~2-day delay between when a flux concentration becomes visible on the Earth-facing solar hemisphere and when it is first assimilated into ADAPT.

To mitigate signal delay issues, Henney2015 implemented a 0-day offset correction for the SIFT forecast models. For each set of daily forecasts, the difference between the model nowcast and associated observation was applied as a constant correction factor to all forecasts made on that day. The 0-day offset technique compensates for local inadequacies in the model while still utilizing the full-Sun nature of ADAPT that enables forecasting. However, the technique applied by Henney2015 requires an observation in each band of the model to determine and apply the corresponding correction. Currently, with aging EUV irradiance observatories and limited EUV spectral coverage (P. Chamberlin et al., 2023), selected bands of EUV observations are not reliably available. It is therefore valuable to apply a similar correction without the need for daily measurements in each EUV band.

The difference between the modeled and observed Mg II (top) and EUV Bands 7, 9, and 26 in Figure 3 appear to correlate somewhat over a solar cycle timescale. This suggests that the errors in the EUV band models could be reduced by applying a time-dependent correction to each band by using the difference between the daily observed and modeled Mg II. We create this correction model by linearly correlating the daily model-observation difference in Mg II with each of the EUV bands such that

$$I_{model}^n - I_{observed}^n = m_3^n (I_{model}^{Mg II} - I_{observed}^{Mg II}) = m_3^n C \quad (4)$$

and then applying this correction term to Equation 3, we get the following

$$I_{corrected}^n = m_0^n + m_1^n S_P + m_2^n S_A - m_3^n C, \quad (5)$$

which yields an Mg II-corrected multiple linear regression for each band. We chose to model the Mg II correction term with only one coefficient, vice a multi-coefficient linear regression, because additional constants were several orders of magnitude smaller than the m_3 correction coefficient, as well as m_0 , m_1 , and m_2 . Therefore, additional coefficients had no effect on model performance or improvement. The coefficients for these models are shown in Table A1 in the appendix. The Mg II correction term on EUV Bands 7 ($m_3^7 C$), 9 ($m_3^9 C$), and 26 ($m_3^{26} C$) are plotted (green) in Figure 4 along with the original model-observation difference (black) from Figure 3. If these

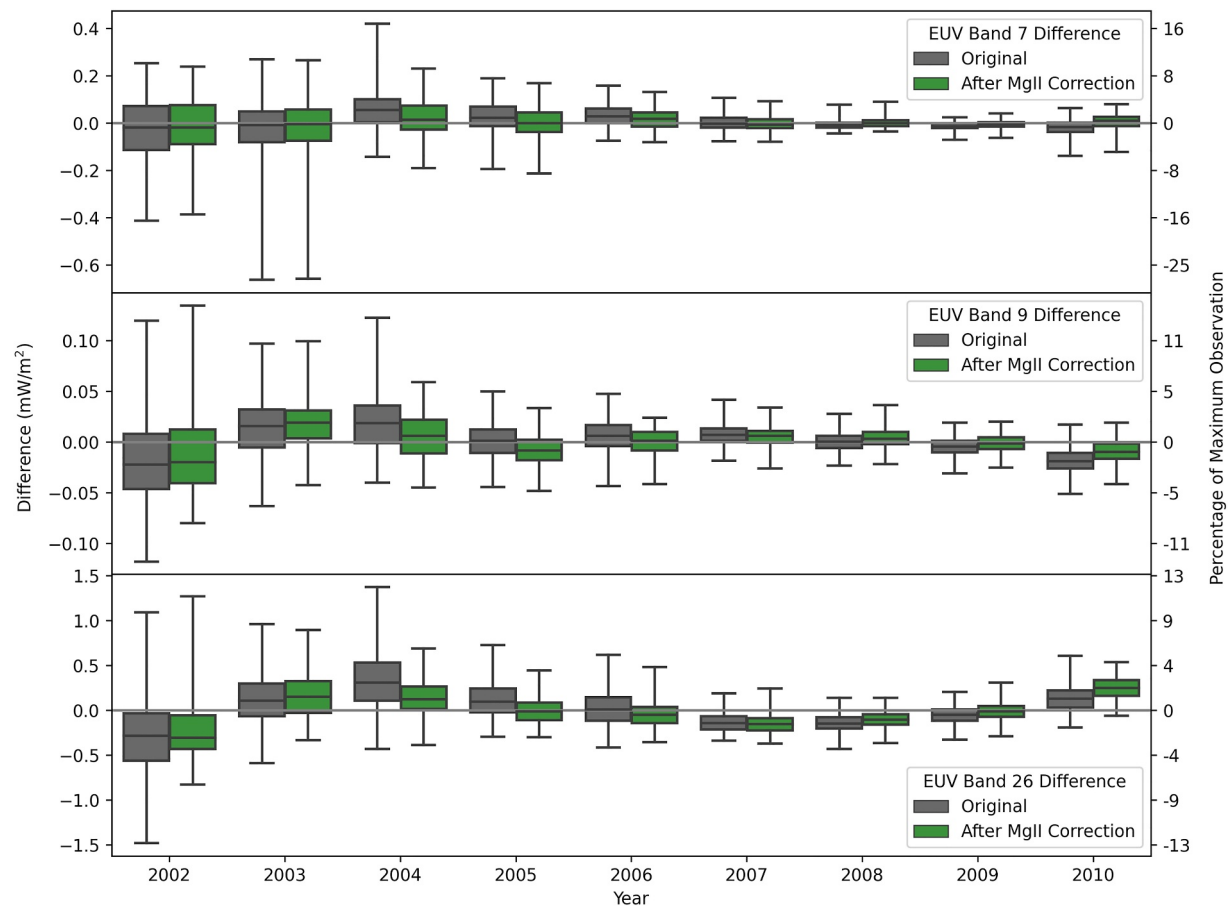


Figure 6. Box and whisker plots for EUV spectral Bands 7, 9, and 26, highlighting the distributions of the difference between the models and observations during the study period. The box indicates the extent of the 25% and 75% quartiles and the line through the box indicates the distribution median over 1 year of data. The whiskers (i.e., the vertical lines) indicate the minimum and maximum. The distributions including the Mg II correction do not strictly improve, however the improvements (e.g., 2004) are much more significant than the occasional times when the distributions worsen. Similar figures for all 37 bands are available at Kniezewski et al. (2023).

points (and lines) overlapped perfectly then the Mg II correction term would allow perfect nowcasting of the EUV band, and anywhere that the two have opposite sign indicates when the Mg II correction harms the nowcast. This correction term does not provide improvements at all times, however, on average the model-observation difference is reduced with this correction.

Improved nowcasting is found to be consistent across all 37 bands as reported in Table 1 and displayed in Figure 5. This shows the Pearson correlation coefficient between both the original and corrected models and the observations of all bands over the entire period studied. The Mg II correction yields improved correlations across all bands, with particular improvement in Band 25 which has the worst correlation. The m_1/m_2 values (see Table A1) also demonstrate why a Mg II correction term is suitable for these models. The m_1/m_2 Mg II and all of EUV band m_1/m_2 values, except for Band 1, are greater than 1, demonstrating that there is a larger dependence on plage regions for the Mg II and the EUV bands. Henney2015 found that m_1/m_2 for $F_{10.7}$ is less than 1, indicating that it is more strongly dependent on active regions. This indicates that the Mg II proxy, rather than the active-region dependent $F_{10.7}$, is more consistent with the behavior of the solar EUV spectrum.

Additionally, Figure 6 exhibits the long-term variability of the EUV Band 7, 9, and 26 models before (gray) and after (green) applying the Mg II offset correction. This plot shows that the error between the observations and

model are typically smaller (i.e., the distribution shifts closer to 0) and the range in variation decreases (i.e., the vertical range of each box is smaller). Interestingly, the overall trend of the model-observation difference over the solar cycle does not change, with the models tending to predict more irradiance than observed during the decline of the solar cycle (2003–2007) and less during the maximum (2002). Warren et al. (2021) identify a similar trend in their models which they attribute to discrepancies in the weak magnetic fields ($B_r < 80$ G) between the full-Sun magnetic maps and the original observed magnetograms. We identify two additional possible explanations for this effect. It could indicate that the conversion of magnetic energy into plasma heating in the solar atmosphere is slightly more efficient during the rising phase and solar maximum (leading to more emission than predicted) than the declining phase (with less emission than predicted). It could also be the result of some other long-term variation in the ADAPT maps. For example, because of the delay between the rotation of magnetic flux onto the Earth-facing hemisphere and the incorporation of this flux into ADAPT, the ADAPT maps in general under-represent the magnetic flux on the Earth-facing hemisphere. This effect will be stronger during the rising phase and maximum of the solar cycle when flux emergence is greatest and therefore more flux appears on the farside and is not included in ADAPT until it rotates into the data assimilation window. A more detailed study is needed to better understand the source of this long-term residual trend (e.g., adding another solar cycle of data analysis and/or using different magnetograph inputs, e.g., SDO/HMI and NSO/GONG).

4. Summary

This study builds on the work of the SIFT model, outlined in Henney2012 and Henney2015, that demonstrated the ability of ADAPT global photospheric magnetic maps to drive irradiance nowcasts and forecasts. The original SIFT EUV forecasts benefited greatly from daily calibration of the models to the observed irradiance which corrected short-term errors between the models and observations. However, for periods without real-time calibrated EUV spectral measurements, the original correction technique is not an option for real-time predictions.

In the study presented here, we develop an alternative implementation of daily corrections that does not rely on current EUV irradiance observations. Instead, the daily model and observation is regularly measured for a proxy, in this case the Mg II index. Then, that Mg II index nowcast offset is scaled and a corresponding correction is applied to each EUV irradiance band independently. Applying this correction term to simple multiple linear regression models yields improved nowcasts across the entire spectral range, with the average Pearson correlation coefficient increasing from 0.962 to 0.969 as represented by the horizontal dashed lines in Figure 5. In this work we use the science-quality Bremen Mg II data set to demonstrate the viability of this technique, but this method can be applied using existing operationally available data products such as the Geostationary Operational Environmental Satellite (GOES) Extreme Ultraviolet and X-ray Sensors (EXIS) Extreme Ultraviolet Sensor (EUVS; Eparvier et al., 2009) Mg II data set which began in 2017. This technique can also easily be extended to forecasting EUV bands to drive terrestrial atmospheric models. It can also be applied as a post-processing term to more complex machine learning techniques where it would serve the same function as a daily correction to the model output. This kind of solar proxy-modeling using deep learning and neural networks has recently shown promising results (e.g., see Stevenson et al., 2022; Daniell & Mehta, 2023).

We also identify a solar-cycle trend in the regression models that typically under-predict the irradiance during solar maximum and over-predict the irradiance during the declining phase. This could indicate deficiencies in the ADAPT maps driving these irradiance nowcasts or an underlying nonlinear conversion of photospheric magnetic energy and chromospheric and coronal heating (e.g., not captured with the simple linear regression models applied here). Future work is needed to better understand the source of the model and observation residuals over the solar cycle such as analyzing an additional solar cycle and using different magnetograph inputs.

Appendix A: EUV Model Coefficients

Coefficients for the SIFT linear regression models defined in Equation 5 are given in Table A1.

Table A1
EUV Model Coefficients, Including the Difference Model Coefficients Using Mg II

Band (n)	m_0	m_1	m_2	m_3	m_1/m_2
Mg II	1.494×10^{-1}	2.044×10^{-3}	5.321×10^{-4}	N/A	3.841
1	-6.375×10^{-9}	1.492×10^{-8}	2.068×10^{-8}	3.620×10^{-6}	0.721
2	-1.811×10^{-7}	6.190×10^{-7}	5.728×10^{-7}	2.065×10^{-4}	1.081
3	-1.393×10^{-6}	2.193×10^{-5}	1.352×10^{-5}	6.112×10^{-3}	1.622
4	1.449×10^{-5}	1.095×10^{-5}	5.350×10^{-6}	2.969×10^{-3}	2.047
5	5.734×10^{-5}	1.891×10^{-5}	9.077×10^{-6}	5.115×10^{-3}	2.083
6	1.054×10^{-4}	4.429×10^{-5}	2.129×10^{-5}	1.212×10^{-2}	2.080
7	3.860×10^{-4}	1.370×10^{-4}	6.407×10^{-5}	3.374×10^{-2}	2.138
8	9.538×10^{-5}	3.947×10^{-5}	3.314×10^{-6}	9.787×10^{-3}	11.910
9	3.916×10^{-4}	5.032×10^{-5}	8.284×10^{-6}	1.453×10^{-2}	6.074
10	2.461×10^{-4}	6.129×10^{-5}	1.234×10^{-5}	1.535×10^{-2}	4.968
11	1.462×10^{-4}	7.596×10^{-6}	4.128×10^{-6}	2.991×10^{-3}	1.840
12	5.954×10^{-5}	1.824×10^{-6}	1.226×10^{-6}	7.773×10^{-4}	1.488
13	3.210×10^{-5}	1.139×10^{-6}	7.029×10^{-7}	5.338×10^{-4}	1.620
14	4.117×10^{-5}	4.389×10^{-6}	7.483×10^{-7}	1.281×10^{-3}	5.866
15	1.148×10^{-4}	1.461×10^{-5}	2.240×10^{-6}	4.173×10^{-3}	6.525
16	5.311×10^{-5}	5.979×10^{-6}	1.019×10^{-6}	1.727×10^{-3}	5.868
17	1.776×10^{-5}	1.731×10^{-6}	3.693×10^{-7}	5.382×10^{-4}	4.687
18	4.001×10^{-5}	3.727×10^{-6}	9.899×10^{-7}	1.182×10^{-3}	3.765
19	1.720×10^{-5}	2.195×10^{-6}	3.766×10^{-7}	7.399×10^{-4}	5.831
20	5.417×10^{-5}	1.105×10^{-5}	1.422×10^{-6}	2.401×10^{-3}	7.769
21	8.049×10^{-5}	1.196×10^{-5}	2.418×10^{-6}	3.241×10^{-3}	4.945
22	8.414×10^{-5}	1.081×10^{-5}	2.200×10^{-6}	3.208×10^{-3}	4.913
23	7.619×10^{-5}	6.424×10^{-6}	1.795×10^{-6}	1.560×10^{-3}	3.579
24	6.830×10^{-5}	5.224×10^{-6}	1.423×10^{-6}	1.358×10^{-3}	3.671
25	1.626×10^{-4}	2.925×10^{-6}	2.125×10^{-6}	4.095×10^{-3}	1.377
26	5.444×10^{-3}	6.080×10^{-4}	3.115×10^{-5}	1.760×10^{-1}	19.519
27	8.198×10^{-4}	6.062×10^{-5}	8.048×10^{-6}	2.913×10^{-2}	7.533
28	1.978×10^{-5}	1.289×10^{-6}	2.281×10^{-7}	4.654×10^{-4}	5.652
29	3.588×10^{-4}	1.945×10^{-5}	5.450×10^{-6}	6.208×10^{-3}	3.569
30	1.812×10^{-4}	8.200×10^{-6}	2.413×10^{-6}	2.307×10^{-3}	3.398
31	2.249×10^{-4}	7.655×10^{-6}	2.082×10^{-6}	1.977×10^{-3}	3.677
32	3.242×10^{-4}	7.213×10^{-6}	2.338×10^{-6}	2.665×10^{-3}	3.085
33	5.609×10^{-4}	1.502×10^{-5}	5.474×10^{-6}	3.504×10^{-3}	2.744
34	7.857×10^{-3}	1.711×10^{-5}	4.471×10^{-6}	4.153×10^{-3}	3.828
35	1.114×10^{-3}	1.854×10^{-5}	5.369×10^{-6}	7.270×10^{-3}	3.454
36	2.053×10^{-3}	2.889×10^{-5}	7.706×10^{-6}	1.113×10^{-2}	3.749
37	3.391×10^{-3}	4.590×10^{-5}	7.587×10^{-6}	2.041×10^{-2}	6.050

Data Availability Statement

The Mg II composite index is provided by the University of Bremen at http://www.iup.uni-bremen.de/gome/solar/MgII_composite.dat. The Mg II index data used in this study along with figures for all 37 EUV bands and the scripts used to create and visualize the SIFT models are available through Zenodo at Kniezewski et al. (2023). The solar magnetic sums based on ADAPT are available through Zenodo at Henney et al. (2023). The EUV irradiances in the 37 bands are provided through Zenodo at R. A. Hock et al. (2023).

Acknowledgments

The ADAPT model development is supported by Air Force Research Laboratory (AFRL), along with AFOSR (Air Force Office of Scientific Research) tasks 18RVCOR126 and 22RVCOR012. The EUV data used in this work was compiled by Rachel Hock (AFRL). This work utilizes data produced collaboratively between AFRL and the National Solar Observatory (NSO). The NSO data used for this work are produced cooperatively by National Science Foundation (NSF) and the NSO. The NSO is operated by the Association of Universities for Research in Astronomy (AURA), Inc., under cooperative agreement with the NSF. The views expressed are those of the authors and do not reflect the official guidance or position of the United States Government, the Department of Defense (DoD) or of the United States Air Force.

References

- Arge, C. N., Henney, C. J., Hernandez, I. G., Toussaint, W. A., Koller, J., & Godinez, H. C. (2013). Modeling the corona and solar wind using ADAPT maps that include far-side observations. In G. P. Zank, et al. (Eds.), *American institute of physics conference series* (Vol. 1539, pp. 11–14). <https://doi.org/10.1063/1.4810977>
- Arge, C. N., Henney, C. J., Koller, J., Compeau, C. R., Young, S., MacKenzie, D., et al. (2010). Air Force Data Assimilative Photospheric Flux Transport (ADAPT) model. In M. Maksimovic, K. Issautier, N. Meyer-Vernet, M. Moncuquet, & F. Pantellini (Eds.), *Twelfth international solar wind conference* (Vol. 1216, pp. 343–346). <https://doi.org/10.1063/1.3395870>
- Barnes, G., DeRosa, M. L., Jones, S. I., Arge, C. N., Henney, C. J., & Cheung, M. C. M. (2023). Implications of different solar photospheric flux-transport models for global coronal and heliospheric modeling. *The Astrophysical Journal*, 946(2), 105. <https://doi.org/10.3847/1538-4357/acba8e>
- Chamberlin, P., Warren, H., Edward, T., Mason, J., Klimchuk, J. e., Jones, A., & Kopp, G. (2023). The next decade of solar ultraviolet spectral irradiance—Continuity, modeling, and physics. *Bulletin of the AAS*, 55. <https://doi.org/10.3847/25c2cfef.a05625a8>
- Chamberlin, P. C., Eparvier, F. G., Knoer, V., Leise, H., Pankratz, A., Snow, M., et al. (2020). The Flare Irradiance Spectral Model-Version 2 (FISM2). *Space Weather*, 18(12), e02588. <https://doi.org/10.1029/2020SW002588>
- Covington, A. E. (1947). Micro-wave solar noise observations during the partial eclipse of November 23, 1946. *Nature*, 159(4038), 405–406. <https://doi.org/10.1038/159405a0>
- Daniell, J. D., & Mehta, P. M. (2023). Probabilistic solar proxy forecasting with neural network ensembles. *Space Weather*, 21(9), e2023SW003675. <https://doi.org/10.1029/2023SW003675>
- De Lafontaine, J., & Garg, S. C. (1982). A review of satellite lifetime and orbit decay prediction. *Proceedings of the Indian Academy of Sciences - Earth & Planetary Sciences*, 5(3), 197–258. <https://doi.org/10.1007/bf02897683>
- Doschek, G. A., & Feldman, U. (2010). Topical review the solar UV-x-ray spectrum from 1.5 to 2000 Å. *Journal of Physics B: Atomic and Molecular Physics*, 43(23), 232001. <https://doi.org/10.1088/0953-4075/43/23/232001>
- Dudok de Wit, T., Kretschmar, M., Aboudarham, J., Amblard, P. O., Auchère, F., & Lilén, J. (2008). Which solar EUV indices are best for reconstructing the solar EUV irradiance? *Advances in Space Research*, 42(5), 903–911. <https://doi.org/10.1016/j.asr.2007.04.019>
- Dudok de Wit, T., Kretschmar, M., Lilén, J., & Woods, T. (2009). Finding the best proxies for the solar UV irradiance. *Geophysical Research Letters*, 36(10), L10107. <https://doi.org/10.1029/2009GL037825>
- Eparvier, F. G., Crotser, D., Jones, A. R., McClintock, W. E., Snow, M., & Woods, T. N. (2009). The Extreme Ultraviolet Sensor (EUVS) for GOES-R. In S. Fineschi & J. A. Fennelly (Eds.), *Solar physics and space weather instrumentation iii* (Vol. 7438). <https://doi.org/10.1117/12.826445.743804>
- Fuller-Rowell, T., Solomon, S., Roble, R., & Viereck, R. (2004). Impact of solar EUV, XUV, and X-ray variations on Earth's atmosphere. In *Solar variability and its effects on climate geophysical monograph* (Vol. 141, pp. 341–354). <https://doi.org/10.1029/141GM23>
- Goncharenko, L. P., Tamburri, C. A., Tobiska, W. K., Schonfeld, S. J., Chamberlin, P. C., Woods, T. N., et al. (2021). A new model for ionospheric total electron content: The impact of solar flux proxies and indices. *Journal of Geophysical Research: Space Physics*, 126(2), e28466. <https://doi.org/10.1029/2020JA028466>
- Harvey, J. W., Branstor, D., Henney, C. J., & Keller, C. U., & SOLIS and GONG Teams. (2007). Seething horizontal magnetic fields in the quiet solar photosphere. *The Astrophysical Journal Letters*, 659(2), L177–L180. <https://doi.org/10.1086/518036>
- Heath, D. F., & Schlesinger, B. M. (1986). The Mg 280-nm doublet as a monitor of changes in solar ultraviolet irradiance. *Journal of Geophysical Research*, 91(D8), 8672–8682. <https://doi.org/10.1029/JD091iD08p08672>
- Henney, C. J., Hock, R. A., Schooley, A. K., Toussaint, W. A., White, S. M., & Arge, C. N. (2015). Forecasting solar extreme and far ultraviolet irradiance. *Space Weather*, 13(3), 141–153. <https://doi.org/10.1002/2014SW001118>
- Henney, C. J., Keller, C. U., Harvey, J. W., Georgoulis, M. K., Hadder, N. L., Norton, A. A., et al. (2009). SOLIS vector spectromagnetograph: Status and science. In S. V. Berdyugina, K. N. Nagendra, & R. Ramelli (Eds.), *Solar polarization 5: In honor of Jan Stenflo* (Vol. 405, p. 47). <https://doi.org/10.48550/arXiv.0801.0013>
- Henney, C. J., Kniezewski, K. L., & Schonfeld, S. J. (2023). ADAPT/sift solar magnetic sums (June 1992 to May 2017) [Dataset]. *Zenodo*. <https://doi.org/10.5281/zenodo.10070554>
- Henney, C. J., Toussaint, W. A., White, S. M., & Arge, C. N. (2012). Forecasting $F_{10.7}$ with solar magnetic flux transport modeling. *Space Weather*, 10(2), S02011. <https://doi.org/10.1029/2011SW000748>
- Hickmann, K. S., Godinez, H. C., Henney, C. J., & Arge, C. N. (2015). Data assimilation in the ADAPT photospheric flux transport model. *Solar Physics*, 290(4), 1105–1118. <https://doi.org/10.1007/s11207-015-0666-3>
- Hock, R. A., Chamberlin, P. C., Woods, T. N., Crotser, D., Eparvier, F. G., Woodraska, D. L., & Woods, E. C. (2012). Extreme Ultraviolet Variability Experiment (EVE) Multiple EUV Grating Spectrographs (MEGS): Radiometric calibrations and results. *Solar Physics*, 275(1–2), 145–178. <https://doi.org/10.1007/s11207-010-9520-9>
- Hock, R. A., Kniezewski, K. L., Schonfeld, S. J., & Henney, C. J. (2023). Binned TIMED/SEE VUV irradiance data (January 2002 to June 2013) [Dataset]. *Zenodo*. <https://doi.org/10.5281/zenodo.10119832>
- Jones, H. P., Duvall, J., Thomas, L., Harvey, J. W., Mahaffey, C. T., Schwitters, J. D., & Simmons, J. E. (1992). The NASA/NSO spectromagnetograph. *Solar Physics*, 139(2), 211–232. <https://doi.org/10.1007/BF00159149>
- Kazachenko, M. D., & Hudson, H. S. (2020). Active region irradiance during quiescent periods: New insights from Sun-as-a-star Spectra. *The Astrophysical Journal*, 901(1), 64. <https://doi.org/10.3847/1538-4357/abada6>
- Klobuchar, J. A. (1985). Ionospheric time delay effects on earth-space propagation. In A. S. Jursa (Ed.), *Handbook of geophysics and the space environment* (pp. 10.84–10.88). Air Force Geophysics Laboratory.

- Kniewski, K. L., Schonfeld, S. J., & Henney, C. J. (2023). "Nowcasting Solar EUV Irradiance with Photospheric Magnetic Fields and the MgII Index" Figures, Scripts, and Data [Dataset]. *Zenodo*. <https://doi.org/10.5281/zenodo.10035713>
- Lilensten, J., Dudok de Wit, T., Kretschmar, M., Amblard, P., Moussaoui, S., Aboudarham, J., & Auchere, F. (2008). Review on the solar spectral variability in the EUV for space weather purposes. *Annales Geophysicae*, 26(2), 269–279. <https://doi.org/10.5194/angeo-26-269-2008>
- McNamara, L. F. (1985). High frequency radio propagation. In A. S. Jursa (Ed.), *Handbook of geophysics and the space environment* (pp. 10.45–10.62). Air Force Geophysics Laboratory.
- Pesnell, W. D. (2016). Watching the Sun from space. *Asian Journal of Physics*, 25(3), 233–265.
- Petrie, G., Criscuoli, S., & Bertello, L. (2021). Solar magnetism and radiation. In N. E. Raouafi, A. Vourlidas, Y. Zhang, & L. J. Paxton (Eds.), *Solar physics and solar wind* (Vol. 1, pp. 83–132). American Geophysical Union (AGU). <https://doi.org/10.1002/9781119815600.ch3>
- Richards, P. G., Fennelly, J. A., & Torr, D. G. (1994). EUVAC: A solar EUV flux model for aeronomic calculations. *Journal of Geophysical Research*, 99(A5), 8981–8992. <https://doi.org/10.1029/94JA00518>
- Skupin, J., Weber, M., Noël, S., Bovensmann, H., & Burrows, J. P. (2005). GOME and SCIAMACHY solar measurements: Solar spectral irradiance and Mg II solar activity proxy indicator. *MemSAIT*, 76, 1038.
- Snow, M., Weber, M., Machol, J., Viereck, R., & Richard, E. (2014). Comparison of Magnesium II core-to-wing ratio observations during solar minimum 23/24. *Journal of Space Weather and Space Climate*, 4, A04. <https://doi.org/10.1051/swsc/2014001>
- Solomon, S. C., & Qian, L. (2005). Solar extreme-ultraviolet irradiance for general circulation models. *Journal of Geophysical Research*, 110(A10), A10306. <https://doi.org/10.1029/2005JA011160>
- Stevenson, E., Rodriguez-Fernandez, V., Minisci, E., & Camacho, D. (2022). A deep learning approach to solar radio flux forecasting. *Acta Astronautica*, 193, 595–606. <https://doi.org/10.1016/j.actaastro.2021.08.004>
- Tapping, K. F. (2013). The 10.7 cm solar radio flux (F10.7). *Space Weather*, 11(July), 394–406. <https://doi.org/10.1002/swe.20064>
- Tiwari, S. K., Thalmann, J. K., Panesar, N. K., Moore, R. L., & Winebarger, A. R. (2017). New evidence that magnetoconvection drives solar–stellar coronal heating. *The Astrophysical Journal*, 843(2), L20. <https://doi.org/10.3847/2041-8213/aa794c>
- Torr, M. R., Torr, D. G., Ong, R. A., & Hinteregger, H. E. (1979). Ionization frequencies for major thermospheric constituents as a function of solar cycle 21. *Geophysical Research Letters*, 6(10), 771–774. <https://doi.org/10.1029/GL006i010p00771>
- Viereck, R., Puga, L., McMullin, D., Judge, D., Weber, M., & Tobiska, W. K. (2001). The Mg II index: A proxy for solar EUV. *Geophysical Research Letters*, 28(7), 1343–1346. <https://doi.org/10.1029/2000GL012551>
- Warren, H. P., Floyd, L. E., & Upton, L. A. (2021). A multicomponent magnetic proxy for solar activity. *Space Weather*, 19(12), e02860. <https://doi.org/10.1029/2021SW002860>
- Woods, T. N., Bailey, S. M., Eparvier, F. G., Lawrence, G. M., Lean, J., McClintock, W. E., et al. (1998). TIMED solar EUV experiment. In C. M. Korendyke (Ed.), *Missions to the Sun II* (Vol. 3442, pp. 180–191). <https://doi.org/10.1117/12.330255>
- Woods, T. N., Eparvier, F. G., Bailey, S. M., Chamberlin, P. C., Lean, J., Rottman, G. J., et al. (2005). Solar EUV Experiment (SEE): Mission overview and first results. *Journal of Geophysical Research*, 110(A1), A01312. <https://doi.org/10.1029/2004JA010765>
- Worden, J., & Harvey, J. (2000). An evolving synoptic magnetic flux map and implications for the distribution of photospheric magnetic flux. *Solar Physics*, 195(2), 247–268. <https://doi.org/10.1023/A:1005272502885>